GISD30: global 30-m impervious surface dynamic dataset from 1985 to 2020 using time-series Landsat imagery on the Google Earth Engine platform

Xiao Zhang[1], Liangyun Liu[1, 2, *], Tingting Zhao[1, 3], Yuan Gao[1], Xidong Chen[1], Jun Mi[1, 2]

1 State Key Laboratory of Remote Sensing Science, Aerospace Information Research Institute, Chinese
Academy of Sciences, Beijing 100094, China

2 University of Chinese Academy of Sciences, Beijing 100049, China

3 College of Geomatics, Xi'an University of Science and Technology, Xi'an 710054, China

* Corresponding author Email: liuly@radi.ac.cn

Abstract

Accurately mapping impervious surface dynamics has great scientific significance and application value for urban sustainable development research, anthropogenic carbon emission assessment and global ecological environment modeling. In this study, a novel and accurate global 30 m impervious surface dynamic dataset (GISD30) for 1985 to 2020 was produced using the spectral generalization method and time-series Landsat imagery, on the Google Earth Engine cloud-computing platform. Firstly, the global training samples and corresponding reflectance spectra were automatically derived from prior global 30 m land-cover products after employing the multitemporal compositing method and relative radiometric normalization. Then, spatiotemporal adaptive classification models, trained with the migrated reflectance spectra of impervious surfaces from 2020 and pervious surface samples in the same epoch for each $5°\times5°$ geographical tile, were applied to map the impervious surface in each period. Furthermore, a spatiotemporal consistency correction method was presented to minimize the effects of independent classification errors and improve the spatiotemporal consistency of impervious surface dynamics. Our global 30 m impervious surface dynamic model achieved an overall accuracy of 91.5% and a kappa coefficient of 0.866 using 18,540 global time-series validation samples. Cross-comparisons with four existing global 30 m impervious surface products further indicated that our GISD30 dynamic product achieved the best performance in capturing the spatial distributions and spatiotemporal dynamics of impervious surfaces in various impervious landscapes. The statistical results indicated that the global impervious surface has doubled in the past 35 years, from 5.116×10^5 km^2 in 1985 to 10.871×10^5 km^2 in 2020, and Asia saw the largest increase in impervious surface area compared to other continents, with a total increase of 2.946×10^5 km^2. Therefore, it was concluded that our global 30 m impervious surface dynamic dataset is an accurate and promising product, and could provide vital support in monitoring regional or global urbanization as well as in related applications. The global 30 m impervious surface dynamic dataset from 1985 to 2020 generated in this paper is free to access at http://doi.org/10.5281/zenodo.5220816 (Liu et al., 2021b).

1. Introduction

Impervious surfaces are usually defined as surfaces "preventing the surface water from penetrating into the ground" and are composed of anthropogenic materials, such as steel, cement, asphalt, bricks and stone (Chen et al., 2016; Weng, 2012; Zhang et al., 2020). Over the past few decades, with the rapid growth of the population and the economy, impervious surfaces have been undergoing dramatic expansion, especially in developing countries (Gong et al., 2019; Kuang, 2020). Based on the statistics of the United Nations in 2014, 54% of the world's total population lives in cities, and this proportion is expected to reach 66% in 2050

40 (Science, 2016). As an indicator of the intensity of human activities and economic development, the dynamic information of impervious surfaces plays a significant role in urban planning (Li et al., 2015), biogeochemical cycles (Zhang and Weng, 2016), greenhouse gas emissions and urban heat island effects (Gao et al., 2012; Zhou et al., 2018), and urban sustainable development pathways (Liu et al., 2020b). Therefore, understanding and quantifying global impervious surface spatiotemporal dynamics is critical.

45 In recent years, with the continuous improvement of remote sensing techniques as well as computer storage and computing capabilities, global impervious surface monitoring has been undergoing a transition from the coarse spatial resolution of 1 km to the fine resolution of 30/10 m (Corbane et al., 2020; Gong et al., 2020; Liu et al., 2018; Liu et al., 2020b; Schneider et al., 2009; Zhao et al., 2020; Zhou et al., 2018). Specifically, coarse impervious surface products primarily use time-series nighttime light datasets (including 50 DMSP and VIIRS NTL imagery) (Xie and Weng, 2017; Zhao et al., 2020) and MODIS imagery (Huang et al., 2020; Schneider et al., 2010) to capture global impervious surface dynamics; for example, Huang et al. (2021) used a fully automated mapping method to produce global 250 m urban area products for 2001 to 2018 using time-series MODIS imagery. Zhou et al. (2018) used the Defense Meteorological Satellite Program/Operational Linescane System's nighttime light data to develop temporally and spatially consistent 55 global 1 km urban maps for 1992 to 2013. Although these coarse global impervious surface dynamic products could capture global urban expansion trends, they are unsuitable for many regional applications, because a large quantity of broken and small-sized impervious surfaces are missed in coarse remote sensing imagery (Gong et al., 2020). Recently, benefiting from the improvements and maturity of cloud computing platforms (such as Google Earth Engine (Gorelick et al., 2017)), many global 30 m multitemporal impervious surface 60 products have been produced using long time-series Landsat imagery (Florczyk et al., 2019; Gong et al., 2020; Liu et al., 2018; Liu et al., 2020b). For example, Liu et al. (2018) proposed a new index to develop multitemporal global 30 m urban land maps for 1990 to 2010 with 5-years intervals. Gong et al. (2020) used a combination of "exclusion–inclusion" and "temporal check" methods to generate an annual global 30 m artificial impervious surface area dataset for 1985 to 2018. However, Liu et al. (2021a) comprehensively 65 reviewed and analyzed the accuracies and spatial consistencies of seven global 30 m impervious surface products, and found significant inconsistency and uncertainty inherent within these datasets, while Zhang et al. (2020) quantitatively evaluated six global 30 m impervious surface products using 11,942 validation samples, finding unsatisfactory accuracies and low levels of agreement between them. Therefore, an accurate global 30 m impervious surface dynamic product using an efficient mapping method is still urgently needed.

70 Over the past few decades, many methods have been proposed for generating regional or global multitemporal impervious surface products. Generally, these methods can be divided into two groups: time-series change detection (Jing et al., 2021; Li et al., 2018; Song et al., 2016) and multitemporal independent classification/extraction (Gong et al., 2020; Liu et al., 2020b; Zhang and Weng, 2016). The time-series change detection strategy used change detection models to determine the break points in 75 continuous Landsat observations. As this strategy makes full use of the correlations inherent within time-series imagery, it has higher robustness and a greater ability to capture urbanization time and frequency (Liu et al., 2019). However, as impervious surfaces are usually nonlinear, with high temporal and spatial heterogeneity, impervious surface monitoring is a highly difficult and challenging task, especially for arid or semi-arid areas (Reba and Seto, 2020; Sexton et al., 2013). Zhu et al. (2019) demonstrated that the newest 80 continuous monitoring of land disturbance (COLD) method still suffer from an omission error of 27% and a

commission error of 28%. Meanwhile, the monitoring efficiency of the time-series change detection strategy is very low, because it uses pixel-by-pixel modeling and continuous Landsat imagery.

The multitemporal independent classification/extraction strategy generates multiple temporally independent impervious surface maps, and then derives "from–to" information through per-pixel comparison, so the means of generating multiple temporally independent impervious surface maps is the key issue of the strategy. Our previous study (Zhang et al. (2020)) concluded that there are three ways to generate independent impervious surface maps including: spectral mixture analysis (Wu, 2004; Zhuo et al., 2018), the spectral index-based method (Gao et al., 2012; Liu et al., 2018) and the image classification method (Zhang and Weng, 2016; Zhang et al., 2020). However, the spectral mixture analysis had great difficulty in finding the optimal endmembers, especially for long time-series monitoring. The spectral index-based method was simpler and more efficient than the other two strategies, but it encountered great difficulty in identifying the optimal threshold for deriving the impervious pixels from pervious surfaces, especially in arid areas (Sun et al., 2019). The image classification strategy uses training samples to build the classifiers for identifying impervious surfaces, and performed well in complex impervious surface mapping (Okujeni et al., 2013; Zhang et al., 2020). However, collecting training samples is a time-consuming and labor-intensive task, especially for large-area time-series impervious surface monitoring. Fortunately, the spectral generalization strategy has been demonstrated to perform very well in automatic land-cover mapping and monitoring (Phalke and Özdoğan, 2018; Woodcock et al., 2001; Zhang et al., 2019). For example, Zhang et al. (2019) employed the reflectance spectra from the earlier MCD43A4 NBAR dataset to automatically generate land-cover maps in China using multitemporal Landsat imagery, and achieved an overall accuracy of 80.7%.

As impervious surfaces are usually nonlinear with high temporal and spatial heterogeneity, impervious surface monitoring is a challenging task. The aim of the study was to automatically produce an accurate and novel global 30 m impervious surface dynamic dataset (GISD30) for 1985 to 2020 by combining time-series Landsat imagery and the spectral generalization method. To achieve this goal, we first migrated the reflectance spectra of the impervious surface and simultaneously transferred the training samples of pervious surfaces to other periods in order to automatically monitor the spatiotemporal dynamic of impervious surface changes from 1985 to 2020. Then, we combined the local adaptive model and time-series Landsat imagery to independently produce impervious surface time-series products. Lastly, a spatiotemporal consistency correction method was applied to independent impervious surface products to minimize the effects of classification errors and ensure the reliability and spatiotemporal consistency of the final dynamic impervious surface dataset. The results indicate that our global 30 m impervious surface dynamic dataset was accurate, and could provide vital support for monitoring regional or global urbanization and performing related tasks.

2. Datasets

2.1 Time-series Landsat imagery

As a single Landsat mission cannot cover the whole period of 1985 to 2020 (Roy et al., 2014), all available Landsat imagery, including Landsat 4, 5, 7 and 8, archived on the GEE computation platform, were collected to monitor the spatiotemporal dynamics of impervious surfaces. To minimize the scattering and absorption effects of the atmosphere, all Landsat imagery was corrected for the surface reflectance using the Land Surface Reflectance Code (LaSRC) (Vermote et al., 2016) and Landsat Ecosystem Disturbance Adaptive Processing System (LEDAPS) (Vermote, 2007) algorithms. Meanwhile, poor observations

(including snow, shadow, cloud and saturated pixels) in the Landsat imagery were masked using the CFmask algorithm (Zhu and Woodcock, 2014), which is the official Landsat processing algorithm and is included in the Landsat Surface Reflectance (SR) Product Handbook (USGS, 2017). Figure 1 illustrates the spatial distributions of all available Landsat observations from 1985 to 2020, with intervals of 5-years; clearly, the
125 availability of Landsat imagery had a significant positive relationship with the advancement of the monitoring period, mainly because later Landsat satellites had greater capacities for onboard recording and satellite-to-ground transmission compared with previous Landsat systems (Roy et al., 2014). In addition, as only Landsat 5 could provide observation imagery, and satellite-to-ground transmission capabilities were fairly low before 2000, the Landsat observations available for before 2000 do not cover the whole world, and
130 those for 1985 are especially limited; however, it should be noted that we assumed that the land-cover in these areas with missing data would remain stable during the period.
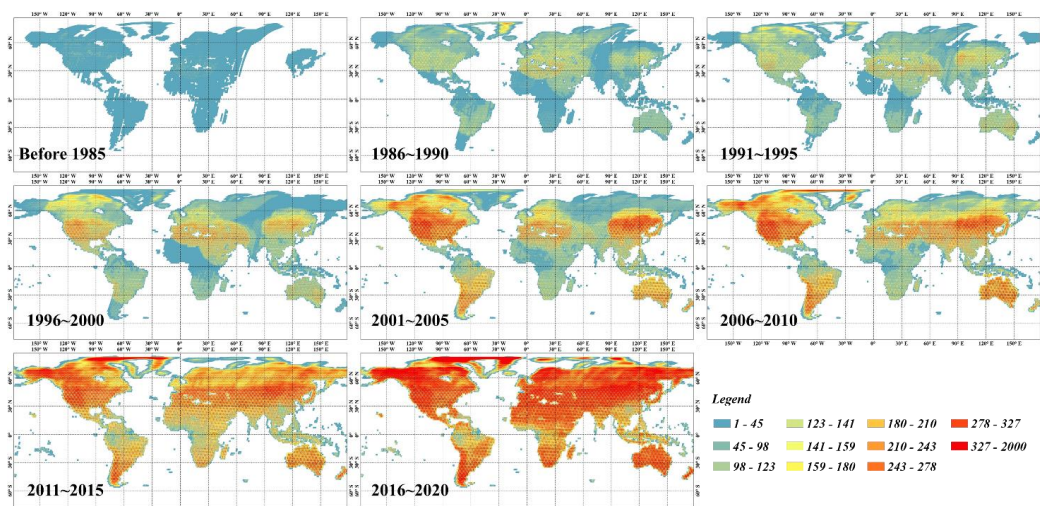

Figure 1. The spatial distributions of the available Landsat observations from 1985 to 2020, with 5-year intervals.

135 **2.2 Global 30 m land-cover product in 2020**

To automatically monitor the spatiotemporal dynamics of impervious surfaces, it was necessary to import a global 30 m land-cover product from 2020, which was used as the reference dataset for training samples in Section 3, and provided the broadest impervious surface information for monitoring spatiotemporal dynamics. In this study, the GLC_FCS30-2020 (Global Land Cover product with Fine Classification System at 30 m in
140 2020) dataset, generated by combining the time-series of Landsat imagery with high-quality training data from the Global Spatial Temporal Spectra Library on the Google Earth Engine computing platform (Zhang et al., 2021), was used, showing an overall accuracy of 82.5% and a kappa coefficient of 0.784 for the level-0 validation system (9 basic land-cover types), and an overall accuracy of 68.7% and kappa coefficient of 0.662 for the UN-LCCS level-2 system (24 fine land-cover types), employing 44,043 global validation samples
145 (Zhang et al., 2021). It should be noted that the impervious surface layer in the GLC_FCS30-2020 dataset was independently produced by combining multisource and multitemporal remote sensing imagery, and achieved

an overall accuracy of 95.1% and a kappa coefficient of 0.898 (Zhang et al., 2020). The GLC_FCS30-2020 dataset is free to access at http://doi.org/10.5281/zenodo.4280923 (Liu et al., 2020a).

2.3 Validation dataset

150   To quantitatively assess the accuracies of our impervious surface dynamic time-series products, 18,540 validation samples (Figure 2), including 8,554 impervious samples and 9,986 pervious samples, covering the long-term time-series from 1985 to 2020, were randomly generated using the stratified random sampling strategy, and further interpreted on the Google Earth Engine computing platform. Using the GEE computing platform had obvious advantages over collecting validation samples, including: 1) storing massive amounts of

155   remote sensing imagery with various spatial resolutions and time spans; 2) easy access to different remote sensing images via simplified coding (Gorelick et al., 2017). Therefore, using multisource high-resolution imagery archived in the GEE platform, each validation sample could be marked as "pervious surface" or "specific change year of impervious surface". However, as the high-resolution images from 1985 to 2000 were sparse, and the Landsat imagery contained observations for that period with satisfactory spatial resolution, we

160   used the time-series Landsat imagery as the auxiliary dataset for visual interpretation between 1985 and 2000. Further, as the spatial heterogeneity of the impervious surface was usually higher than that of natural land-cover types, and land-cover transition areas were often more prone to confusion, the location of each validation sample in rural areas was moved to the center of the impervious object (such as buildings and roads), and the impervious area in a 30×30 m window should comprise more than 50% when identifying

165   impervious samples (Zhang et al., 2020). Lastly, to minimize the influence of the interpreting experts' subjective knowledge, each validation sample was to be independently interpreted by five experts.
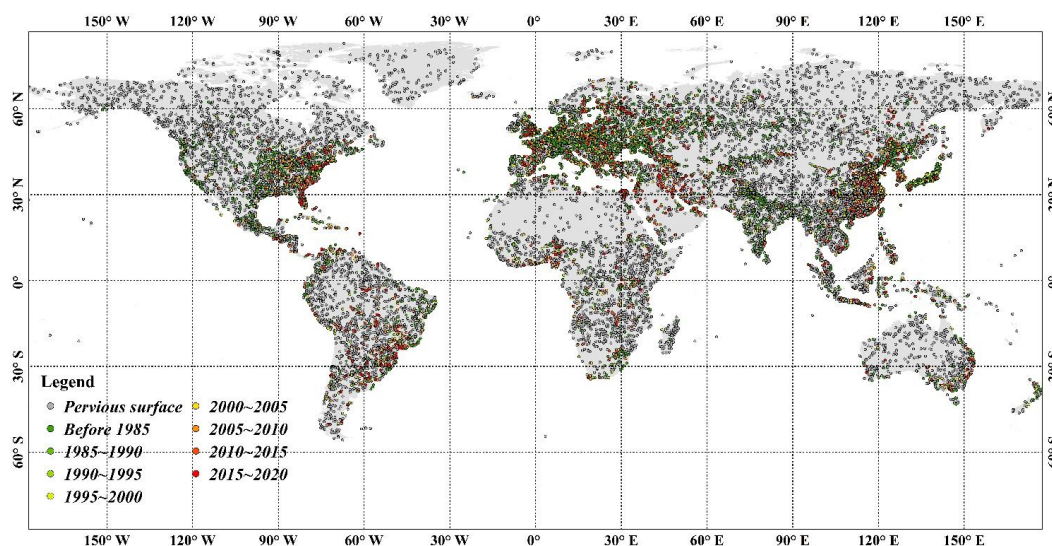

Figure 2. The spatial distribution of the global multitemporal impervious surface validation dataset for 1985-2020.

170   ## 2.4 Existing multitemporal global 30 m impervious surface products

Earth System
Science
Data

Open Access

Discussions

In this study, four existing multitemporal global 30 m impervious surface products, including GAIA (Global Artificial Impervious Area), GHSL (Global Human Settlement Layer), GlobeLand30 impervious surface layer and NUACI (Normalized Urban Areas Composite Index) -based maps, were used to comprehensively analyze the performance of our products. Specifically, GAIA was generated by combining
175 the "Exclusion/Inclusion" and "Temporal Consistency" methods and applying them to time-series Landsat imagery, which provided the global annual impervious surface from 1985 to 2018 at a 30 m spatial resolution, with a mean accuracy of 90% using 3500 validation samples (Gong et al., 2020).

Furthermore, the GHSL products, developed by fusing supervised and unsupervised classification processes to achieve a combination of data-driven and knowledge-driven processes, contained four epochs'
180 impervious surface dynamics (1970, 1990, 2000 and 2015) (Florczyk et al., 2019; Pesaresi et al., 2016), with the high overall accuracy of 96.28% and the low kappa coefficient of 0.323, verified using the open LUCAS (Land-Use/Cover Area Frame Survey) validation dataset for Europe (Pesaresi et al., 2016).

Thirdly, the GlobeLand30 impervious surface layer, which was an independent land-cover type in the GlobeLand30 global land-cover product, was produced by combining pixel-based classification, multi-scale
185 object-oriented segmentation and manual verification based on the visual interpretation of high-spatial resolution imagery (Chen et al., 2015). Meanwhile, to eliminate salt and pepper noise in the impervious surface layer, a minimum unit of 4 ×4 pixels was applied for each impervious surface object. In this study, three epochs' (2000, 2010 and 2020) impervious surface layers were included in the GlobeLand30, and independent validation indicated that the accuracy of impervious surface identification was over 80% (Chen
190 and Chen, 2018; Chen et al., 2016).

Lastly, NUACI-based products were generated by combining the multi-temporal NUACI index and adaptive threshold optimization methods and applying them to the time-series Landsat and nighttime light imagery (Liu et al., 2018), which contained the impervious surface dynamics of seven epochs from 1985 to 2015, with five-year intervals. Further, independent validation indicated that the NUACI-based products
195 achieved overall accuracy, producer's accuracy and user's accuracy of 0.81–0.84, 0.50–0.60 and 0.49–0.61, respectively, at the global level (Liu et al., 2018).

3. Methods

To automatically monitor the spatiotemporal dynamics of impervious surfaces, a temporal spectral generalization method has been proposed in Figure 3. First, the training samples and maximum impervious
200 surface area in 2020 were automatically derived from the earlier GLC_FCS30-2020 land-cover products. Secondly, based on the assumption that the land-cover transition from impervious surface to pervious surface was irreversible, the pervious surface samples in 2020 could be directly transferred to other periods. As for the impervious surface samples, as it was impossible to directly transform them, we migrated their reflectance spectra from 2020 to other periods to achieve the automatically monitored spatiotemporal dynamics. Thirdly,
205 multitemporal local adaptive random forest classification models, trained by the migrated reflectance spectra of impervious and pervious surface samples, were applied to independently generate impervious time-series surface maps from 1985 to 2015. Lastly, the temporal consistency checking method was used to ensure the spatiotemporal consistency and logic of using this approach for monitoring the spatiotemporal dynamics of impervious surfaces.
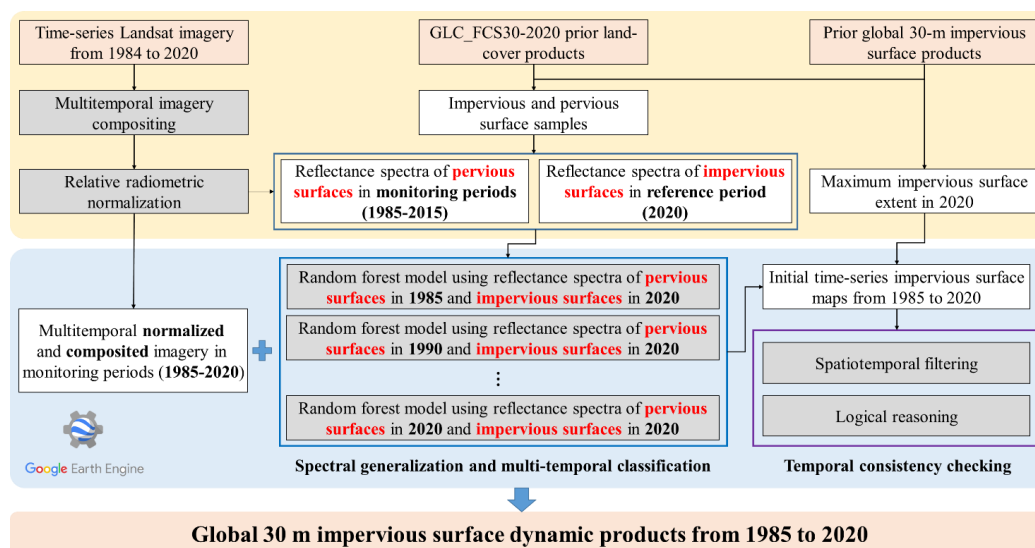
Figure 3. The flowchart of the spectral generalization method for automatically monitoring the spatiotemporal dynamics of impervious surface from 1985 to 2020.

3.1 Deriving training reflectance spectra and maximum impervious surface area

To achieve the automatic monitoring of the spatiotemporal dynamics of impervious surfaces, two key measures should be taken, including: 1) ensuring the spectral consistency between reference period and other periods, which guarantees the feasibility of migrating the reflectance spectra of impervious surfaces in 2020 to other periods; 2) automatically deriving training samples and maximum impervious surface extent from the GLC_FCS30 products and other impervious surface products.

3.1.1 Multitemporal imagery composting and relative radiometric normalization

As our previous work (Zhang et al. (2020)) had quantitatively demonstrated that multitemporal information made a positive contribution to large-area impervious surface mapping, and the availability of Landsat imagery varied with the spatial distribution in Figure 1, it was necessary to decompose the time-series Landsat imagery into multitemporal features. Our previous work (Zhang et al. (2021)) concluded that there were two main options—"selection-based" and "transform-based"—for extracting multitemporal information from time-series imagery. Specifically, the "selection-based" option involved using user-defined criteria to select the most suitable observation from the time-series imagery. For example, the maximum NDVI (Normalized Difference Vegetation Index) compositing method was used to select the observation with the largest NDVI from the pixel-by-pixel and time-series observations. Therefore, "selection-based" composited imagery can still be used to characterize the actual reflective properties of the land surface. Furthermore, the "transform-based" method uses the transform models (Fourier transform, mathematical statistics, etc.) to composite the time-series observation band by band; for example, Zhang et al. (2020) used the statistical quantile method to extract multitemporal information from time-series Landsat imagery. However, it should be noted that "transform-based" composited imagery cannot give the actual characteristics of the land surface, especially in the spectral dimension.

235   In this study, we migrated the reflectance spectra of impervious surfaces in 2020 to other periods; therefore, the "selection-based" method was the optimal solution. To select the user-defined criteria to composite the multitemporal features, given that the best-available-pixel (BAP) method could simultaneously take into account four factors (sensor type, day of year, distance to cloud or cloud shadow and aerosol optical thickness (White et al., 2014)), it has been widely used for generating annual or seasonal cloud-free

240   composited imagery (Chen et al., 2021; Liu et al., 2019). In this study, in order to further capture the multitemporal information from the time-series Landsat imagery, the seasonal BAP composited method, which applies the BAP compositing approach for each season, was used on time-series Landsat imagery in each period. Therefore, we derived four sets of seasonally composited Landsat imagery for each period. In addition, for each set of seasonally composited imagery, excluding those in six optical bands (blue, green, red,

245   NIR, SWIR1 and SWIR2), three spectral indexes, including the normalized difference built-up index (NDBI), normalized difference water index (NDWI) and NDWI, were also imported, because some studies have demonstrated that these indexes help in identifying impervious surfaces (Liu et al., 2018; Zhang et al., 2020). Eventually, a total of 36 multitemporal spectral bands were derived using continuous 5-year Landsat imagery for each period (Figure 1). It should be noted that we assumed that the land-cover in those areas with missing

250   would remain stable during this period.

In our previous works (Zhang et al., 2019; Zhang et al., 2018), we demonstrated that the spectral consistency between the reference period and other periods would affect the capacity for spectral generalization. In this study, some measures were taken to ensure the highest possible spectral consistency in the Landsat composited imagery for the reference period and other periods: 1) the "selection-based" strategy

255   was applied to ensure that the composited imagery could characterize the reflective characteristics of the land surface; 2) the seasonal BAP method was used to guarantee the phenological consistency of each set of seasonally composited imagery. However, was a small difference in the spectral response between Landsat sensors (TM, ETM+ and OLI) (Roy et al., 2016), and some factors (including the number of available Landsat observations, frequency of cloud and shadow, etc.) caused small temporal difference in the seasonal

260   composites between the reference period and the other periods. Therefore, to further ensure the spectral consistency of each seasonal composite, the relative radiometric normalization method was applied before deriving training reflectance spectra. Specifically, as we migrated the reflectance spectra of impervious surfaces from 2020 to other periods, the seasonal composites in 2020 were the dependent variables ($\rho_R(\lambda_i)$):

$$\rho_R(\lambda_i) = \alpha_i \times \rho_t(\lambda_i) + \beta_i$$

265   where $\rho_t(\lambda_i)$ is the surface reflectance in band λ_i in the period t ($t = 1985, 1990, \dots, 2015$), and α_i and β_i are the slope and intercept of the linear regression model.

3.1.2 Deriving training samples and maximum impervious surface extent

As opposed to the traditional method of collecting training samples based on visual interpretation, in this study, the global training samples, including those of the impervious surface and the pervious surface, were

270   automatically derived from the earlier GLC_FCS30-2020 land-cover products. Specifically, our previous work (Zhang et al. (2020)) concluded that the pervious surfaces contained several land-cover types (cropland, forest, grassland, bare land, etc.) and some of them shared similar spectral characteristics with the impervious surfaces. For example, bare land was spectrally similar to the high-reflectance impervious surfaces because composition materials of the impervious surface, including the cement bricks and stone, were also present in

275   the bare land. Meanwhile, cropland was also easily confused with impervious surfaces, especially in the cases of some rural buildings (Sun et al., 2019), because both are composed of low-reflectance vegetation and high-reflectance artificial materials, or bare soil. Therefore, it was necessary to split the pervious surfaces into three sub-classes (cropland, bare land and other pervious surfaces) when deriving training samples.

    In addition, some studies have quantitatively demonstrated that the distribution, balance and size of
280   training samples affect the classification accuracy (Jin et al., 2014; Mellor et al., 2015; Zhu et al., 2016). For example, Jin et al. (2014) compared two sample allocation processes (proportional to area and equal allocation), and found that proportional allocation achieved a better performance than equal allocation; however, the impervious surface comprised more sparse land-cover types compared to the pervious surfaces in this study. Therefore, similar to our previous work on global impervious surface mapping (Zhang et al.,
285   2020), training samples with equal allocation were used here to guarantee training sample balance and to capture as effectively as possible the spectral heterogeneity of impervious surfaces. Meanwhile, as the spatial distribution of impervious surfaces varies in different regions, and we derived training samples on a global scale, the continents with more sparse impervious surfaces (South America, Africa and Oceania) would lack sufficient samples to characterize their impervious surfaces. In order to further ensure that the training samples
290   were locally adaptive, we adopted the tiled solution used in (Zhang et al., 2021), splitting the global land-area into approximately 961 5°×5° geographical tiles (Figure 4), and independently deriving training samples for each geographical tile. Furthermore, the impervious layer in the GLC_FCS30 was shown to have a user's accuracy of 93.2% and a producer's accuracy of 94.8% (Zhang et al., 2020), which guarantees the reliability of the impervious training samples. To further improve the accuracy of the training samples, corrosion
295   morphological filtering with 3×3 pixels window was applied to the previous impervious layer, because a large number of mixed pixels and misclassifications usually occur at the boundaries of impervious objects. Further, as for the collection of pervious samples, corrosion morphological filtering with a 3×3 pixels window was also used on the GLC_FCS30-2020 land-cover products; then, the three sub-classes of pervious samples (cropland, bare land and other pervious surfaces) were automatically sampled from the filtered
300   GLC_FCS30 products.

    Lastly, although the impervious layer in GLC_FCS30-2020 had an omission error of only 5.2% (Zhang et al., 2020), we still combined multiple global 30 m impervious surface products (GAIA-2018, GHSL-2014, GlobeLand30-2020 and impervious layer in GLC_FCS30-2020) to capture all the impervious surfaces as effectively as possible. Therefore, the maximum area of impervious surface, derived via the union of these
305   four global impervious surface products, was used as the boundary of subsequent time-series-independent classifications.

3.2   Spectral generalization classification and temporal consistency checking

    As mentioned before, the reflectance spectra of impervious surfaces in 2020 were migrated to other periods, while the pervious samples in 2020 could be directly transferred to other periods because of the
310   irreversibility assumption. As opposed to traditional spectral generalization classification methods, which temporally migrate the reflectance spectra of all land-cover types (Zhang et al., 2019), in this study, we needed to independently train the classification models at each period because the reflectance spectra of the pervious surfaces varied with the period. In addition, our previous work (Zhang et al., 2021) concluded that there are two options for large-area or global-scale classification, including global classification modeling and
315   local adaptive modeling. The global modeling strategy, using all training samples to build a single

classification model and then applying the model for the whole world, usually had greater classification efficiency and lower sample size requirements than local adaptive modeling (Zhang and Roy, 2017). Local adaptive modeling firstly splits the large area into multiple local regions, and then independently trains the classification models in each region using corresponding regional samples. Zhang and Roy (2017) and Radoux et al. (2014) quantitatively compared these two modeling strategies, and found that local adaptive modeling performed better than global modeling, because the former increased the sensitivity and fitting ability of the model for the region. Therefore, similar to in our previous work on global land-cover mapping (Zhang et al., 2021), the global land-area was divided into 961 5°×5° geographical tiles (Figure 4) for local adaptive modeling.
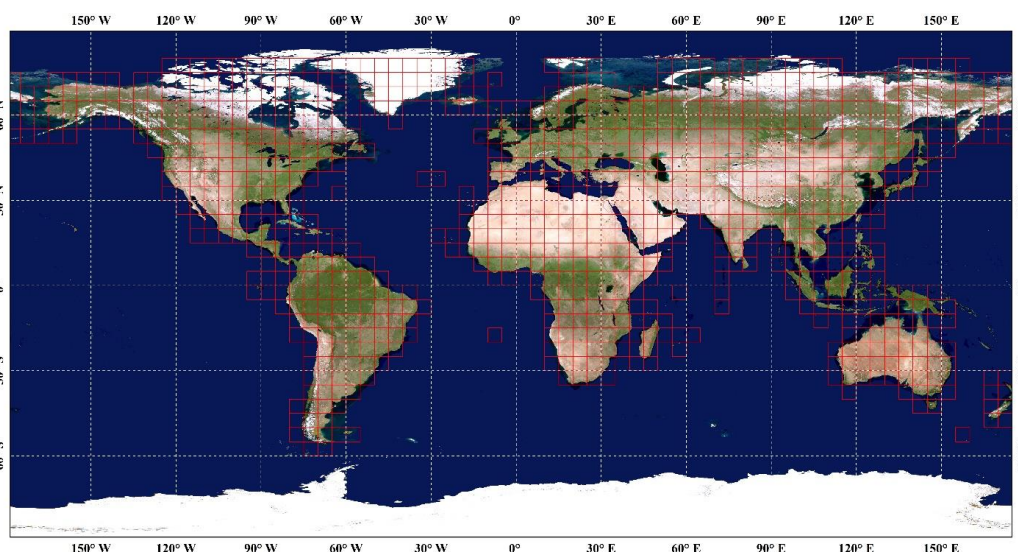

Figure 4. The spatial distribution of 961 5°×5° geographical tiles for local adaptive modeling. The background imagery comes from the National Aeronautics and Space Administration (https://visibleearth.nasa.gov).

Furthermore, the random forest (RF) classification model has significant advantages over other classification models (such as decision tree, support vector machine and neural network), including: 1) higher computation efficiency and classification accuracy; 2) a stronger ability to process high-dimensional data and resist training sample errors; 3) simpler parameter settings (Belgiu and Drăguţ, 2016; Du et al., 2015; Gislason et al., 2006). Therefore, the RF classifier was selected to produce our impervious surface dynamic time-series products. The RF classifier only contains two adjustable parameters (the number of decision trees (Ntree) and the number of selected prediction variables (Mtry)), and Belgiu and Drăguţ (2016) quantitatively analyzed the relationship between the classification accuracy and these two parameters, finding that the Ntree had a greater impact on classification accuracy than Mtry and suggesting that these two parameters should take default values. As such, we defined the Ntree as 500 and Mtry as the square root of the total number of input features.

Lastly, as the impervious surface time-series products were produced by independent classification, it was necessary to use the post-processing method to optimize the impervious time-series products from 1985 to 2020 and minimize the influence of classification error. Over the past few years, many post-processing methods have been proposed, including maximum a posteriori Markov random fields (Cai et al., 2014) and

temporal consistency checks (Li et al., 2015), both of which use contextual spatiotemporal information and prior knowledge to reduce the illogical land-cover transitions caused by classification error. In this study, the "temporal consistency correction" proposed by (Li et al., 2015) was applied to optimize our impervious

345   time-series products. This mainly comprised procedures of spatiotemporal filtering and illogical transition checking, the former of which iteratively calculates the probability of the same land-cover pixels occurring in the neighborhood so as to reduce the influence of classification error caused by individual classifications, and the latter mainly employed the irreversibility assumption to remove illogical transitions from impervious surface to pervious surface.

350   **3.3   Accuracy assessment**

To comprehensively assess the performance of our global 30 m impervious surface dynamic dataset, sample-based and comparison-based methods were applied. Specifically, the sample-based validation method used the multitemporal impervious surface validation samples to calculate four accuracy metrics, including the overall accuracy and kappa coefficient, the producer's accuracy (measuring the omission error) and the user's

355   accuracy (measuring the omission error) (Olofsson et al., 2014). Meanwhile, as opposed to traditional period-by-period accuracy assessments, we categorized the time-series impervious surface dynamic into 9 independent strata, including: pervious surfaces, impervious surfaces before 1985, and expanded impervious surfaces during 1990-1995, 1995-2000, 2000-2005, 2005-2010, and 2015-2020. We then calculated a comprehensive confusion matrix for these nine strata.

360   In addition, the comparison-based method used four global 30 m impervious surface products (GAIA, GHSL, NUACI and GlobeLand30) with multiple epochs as the comparative dataset for analyzing the performance of our GISD30 products. Specifically, we compared the time-series impervious areas of five products in six continents, and further analyzed the spatial consistency between GISD30 and four comparative datasets at the global scale. Further, we selected three types of cities (mega-cities, tropical cities and arid cities)

365   to illustrate the performance of five global 30 m impervious surface products used for capturing the spatiotemporal dynamic.

4   Results

4.1   The spatiotemporal dynamics of impervious surfaces from 1985 to 2020

Figure 5 illustrates the spatial distributions of global 30 m impervious surface time-series maps for

370   1985-2020, with intervals of 5 years. Intuitively, as the world's main impervious surfaces and economic activities are concentrated in the northern hemisphere, the intensity of impervious surface expansion in the northern hemisphere was more significant than that in the southern hemisphere. Furthermore, the impervious surfaces have undergone rapid urbanization in past 35 years, especially in Asia. For example, the impervious surface areas in India and China in 1985 were mostly low, but many low-density areas (including southeast

375   China, central India, etc.) were transformed into high-density regions by 2020.
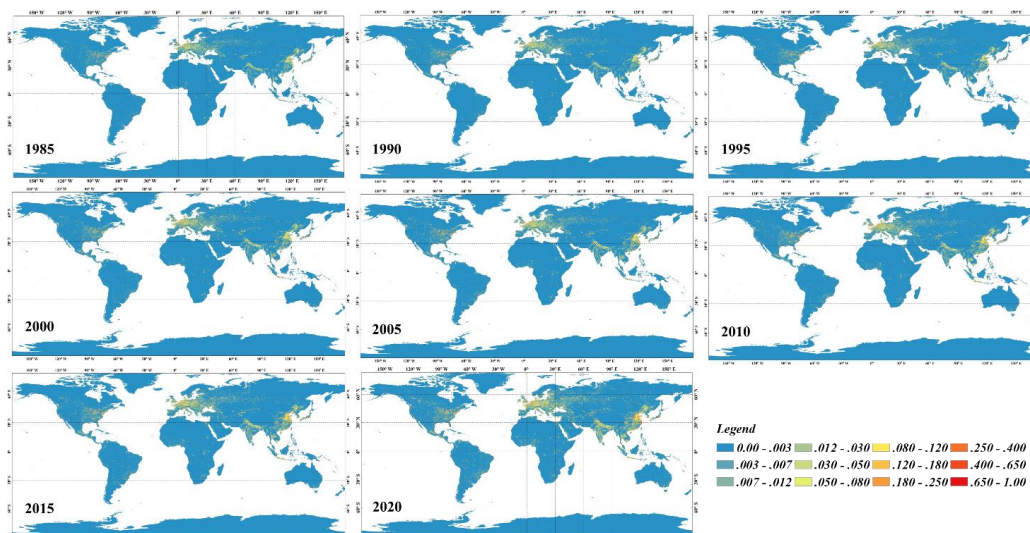
Figure 5. The spatial distributions of global 30 m impervious surface time-series results from 1985 to 2020 with intervals of 5 years. Each pixel represents the fraction of impervious surface within each 0.05°×0.05° spatial unit.

380   Figure 6 quantitatively summarizes the impervious surface areas and their changes on six continents from 1985 to 2020. Overall, the global impervious surface area has doubled in the past 35 years, from 5.116×10^5 km^2 in 1985 to 10.871×10^5 km^2 in 2020. Specifically, Asia experienced the largest increase in impervious surface area compared to other continents, with a total increase of 2.946×10^5 km^2 (from 1.908×10^5 km^2 in 1985 to 4.854×10^5 km^2 in 2020), followed by North America (from 1.202×10^5 km^2 to 2.188×10^5 km^2), Europe

385   (from 1.330×10^5 km^2 to 2.168×10^5 km^2), Africa (from 0.264×10^5 km^2 to 0.725×10^5 km^2), and South America (from 0.298×10^5 km^2 to 0.735×10^5 km^2), and Oceania experienced lowest urbanization, with an increase of 0.088×10^5 km^2 over the past 35 years. In addition, the proportion of impervious area on three continents, namely, Asia, Africa and South America, obviously increased, and the proportions of the remaining three continents (Europe, North America and Oceania) declined (Figure 6b). Specifically, the proportion of

390   impervious area in Asia increased the most, from 37.3% to 44.7%, while the proportion in Europe clearly decreased, from 26.0% to 20.1%. Lastly, Figure 6d illustrates the impervious surface expansion ratio of six continents in 1985-2020. Africa displayed the fastest expansion ratio compared to other continents—the impervious area in Africa was 1.74 times greater than that in 1985, followed by Asia and South America, with expansion ratios of 154.4% and 146.4% over the period, respectively. Comparatively, as Europe and North

395   America had large impervious surface areas in 1985, their impervious area expansion ratios were relatively low. Meanwhile, the expansion rate of impervious surface area on six continents after 2000 was significantly faster than before 2000.
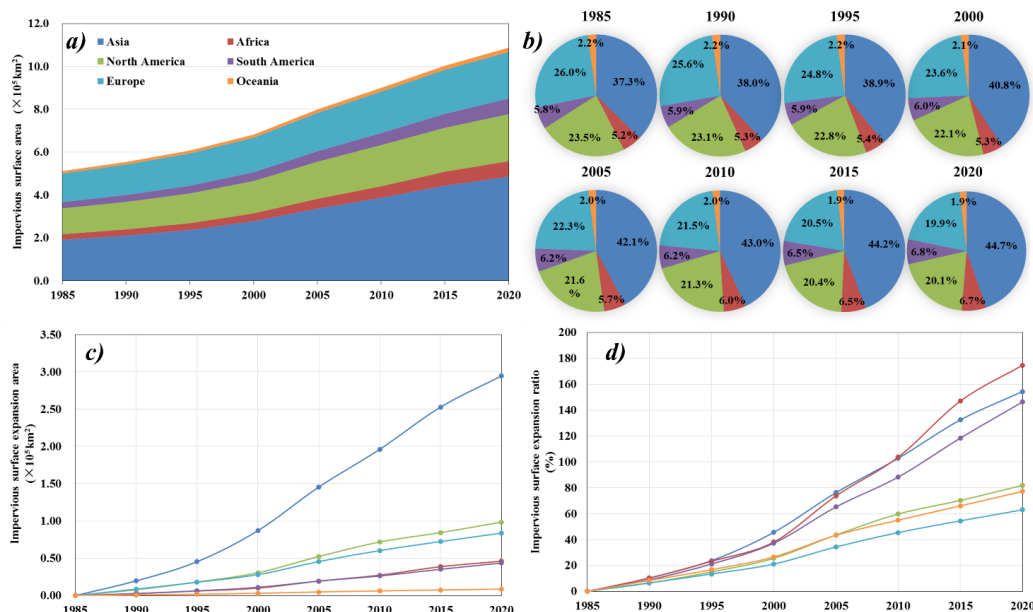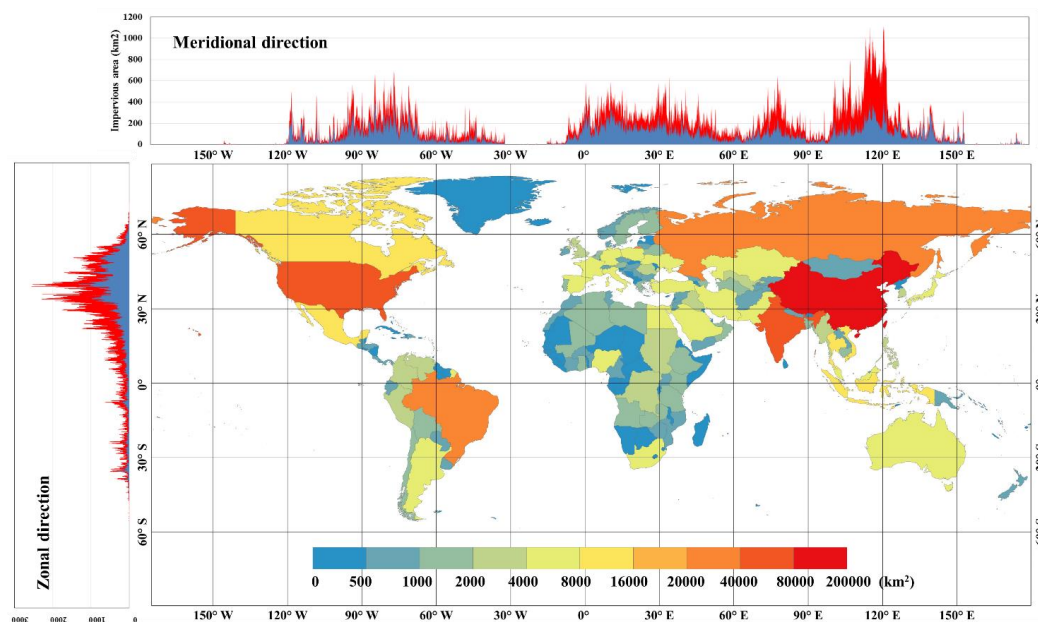
Figure 6. The expansion of impervious surfaces on each continent over the period of 1985-2020. (a) The impervious areas of six continents in each period. (b) The proportion of impervious areas on six continents from 1985 to 2020. (c-d) The increased impervious area and corresponding expansion ratio on each continent.

Figure 7 quantitatively measures the growth of impervious surfaces in various countries around the world over the period of 1985-2020. China underwent the largest increase in impervious area in the last 35 years, with an increase of 1.31×10^5 km^2, followed by America and India both exceeding 4.0×10^4 km^2, and Russia and Brazil exceeding 2.0×10^4 km^2. Meanwhile, from the perspective of spatial distribution, countries in Asia and North America displayed a higher increase in impervious area than those in other continents, especially East Asian and South Asian countries. In comparison, most countries in Africa underwent relatively little impervious surface growth, with an increase of less than 4000 km^2 over the past 35 years. Although Europe is a center of global economic activity, the increased impervious area in European countries was not significant compared with North America and Southeast Asia, and the average increase in area was less than 8000 km^2. In addition, Figure 7 shows the sum of the impervious surface area in the meridional and zonal directions in 1985 (blue) and 2020 (red), with a step of 0.05°, respectively. Firstly, the meridional statistics indicate that the impervious surface in 1985 was more evenly distributed in the meridional direction than that in 2020. In 2020, there were four distinct peak intervals: 100°W~70°W (covering eastern United States), 0°~50°E (containing most European countries), 70°E~90°E (covering the whole of India) and 100°E~120°E (containing many Southeast Asia countries and China). Meanwhile, the increase in impervious area in the Eastern Hemisphere was significantly larger than that in the Western Hemisphere, and the maximum increase in impervious area was located near 120°E, containing China's three major economic deltas (Yangtze River Delta, Pearl River Delta and Jing-Jin-Ji metropolitan region). Next, the zonal statistics indicate that the vast majority of impervious surfaces in the world are distributed between approximately 20°N and 60°N, the area of which contains most of the world's economically developed and high-density countries. Similarly, the increase in

impervious area over the past 35 years was also concentrated in the Northern Hemisphere, and the increase between 20°N~60°N accounted for 70.75% of the total increase in the world.

Figure 7. The expansion of impervious area in each country over the period 1985-2020, and meridional and zonal impervious area statistics for 1985 (blue) and 2020 (red), with a step of 0.05°.

4.2 Accuracy assessment using validation samples

Table 1 quantitatively assesses the performance of our time-series global impervious surface dynamic products using 18,540 multitemporal validation samples. The global impervious dynamic products achieved the overall accuracy of 91.5% and a kappa coefficient of 0.866 in the nine-strata validation system. Specifically, from the perspective of user's accuracy, the pervious surface had the highest accuracy (98.5%) because we used the maximum impervious area in 2020 to monitor the impervious surface dynamics, and the prior impervious layer in GLC_FCS30-2020 also had the high user's accuracy of 93.2% (Zhang et al., 2020). The impervious surface before 1985 achieved an accuracy of 92.4%, mainly because the stable impervious area in 1985 was obviously larger than the expanded area over each 5-year period, and capturing the expansion impervious surface was also more difficult. Furthermore, the measurements of expansion in impervious surfaces in seven 5-year periods had similar performances, with an accuracy of approximately 72%. Confusion mainly occurred in temporally adjacent periods because the transition from a pervious surface to impervious surface is a slow process and spans a long period of time, which directly increases the difficulty of monitoring it. In addition, the producer's accuracy had a similar distribution law to the user's accuracy for each strata in Table 1. However, the producer's accuracy for the expansion of impervious surface after 2000 was higher than that before 2000, which was mainly affected by the available Landsat observations shown in Figure 1. Similarly, Gong et al. (2020) also found that the monitoring uncertainty before 2000 was greater than after 2000.

Earth System
Science
Data

Open Access

Discussions

445 Table 1. The confusion matrix of our global 30 m impervious surface dynamic products using 18,540 validation samples.

	P.S.	1985	85~90	90~95	95~00	00~05	05~10	10~15	15~20	Total	U.A.
P.S.	9840	11	20	14	22	21	14	24	20	9986	0.985
1985	200	4140	31	41	36	12	14	4	2	4480	0.924
85~90	10	70	252	10	3	4	2	1	0	352	0.716
90~95	21	42	16	259	12	5	1	3	0	359	0.721
95~00	36	68	10	23	418	11	9	6	4	585	0.715
00~05	56	40	8	30	34	587	25	14	5	799	0.735
05~10	30	37	8	14	14	32	511	18	4	668	0.765
10~15	36	47	7	11	16	22	47	528	11	725	0.728
15~20	39	56	5	2	9	8	12	34	421	586	0.718
Total	10268	4511	357	404	564	702	635	632	467	18540	
P.A.	0.958	0.918	0.706	0.641	0.741	0.836	0.805	0.835	0.901		
O.A.	0.915										
Kappa	0.866										

Note: P.S.: pervious surface; 1985: impervious surface before 1985; 85~90: expansion of impervious surface during 1985~1990; …, 15~20: expansion of impervious surface during 2015~2020; U.A.: user's accuracy; P.A.: producer's accuracy; O.A.: overall accuracy.

450   Figure 8 illustrates the confusion proportions of the pervious surface, the stable impervious surface and the expanded impervious surface over each 5-year period, according to the confusion matrix in Table 1. Obviously, the pervious surface and stable impervious surface before 1985 had the lowest confusion proportions, because we already knew the maximum impervious surface area for 2020. Next, the confusion proportion between the expansion of impervious surface before 2000 and the stable impervious surface in

455 1985 was approximately 10~20%, mainly because the Landsat imagery before 2000 was sparse, and we assumed that the land-cover in areas missing Landsat data would remain stable. Furthermore, there was also a certain degree of confusion between the expanded impervious surface and the pervious surface (approximately 5%), because urbanization generally occurred on the peripheries of cities, and thus was more likely to be confused with pervious surfaces. Lastly, there was also much confusion between seven periods of impervious

460 surface expansion, especially for the three temporally adjacent periods, because the transition from pervious surface to impervious surface is a long and slow process. Similarly, Liu et al. (2019) used the continuous change detection method to capture impervious surface dynamics and found a temporal bias between the detected change time and the actual change time.
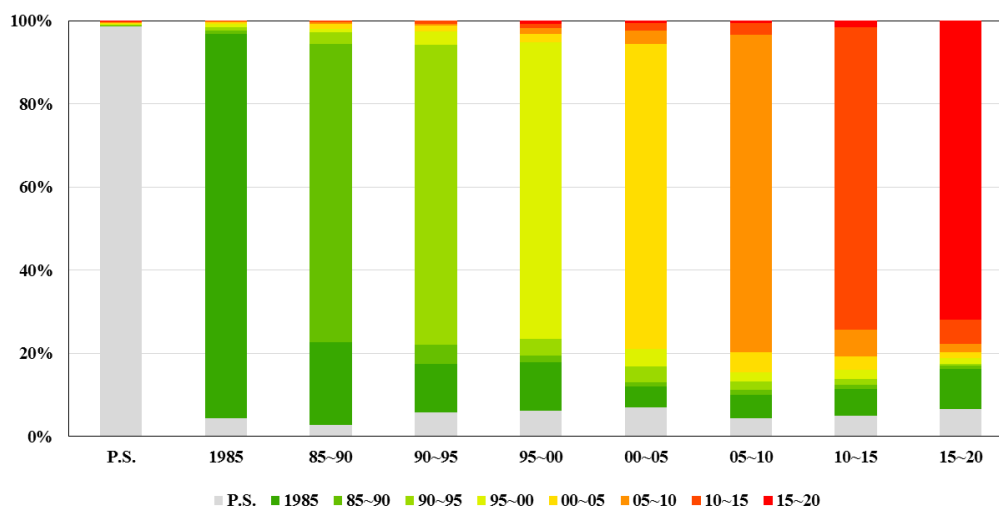
465   Figure 8. The confusion proportions of pervious surfaces, impervious surfaces in 1985, and increased impervious surfaces from 1985 to 2020.

4.3   Cross-comparisons with other global 30 m impervious surface products

4.3.1 Cross-comparison at global scale

        To comprehensively analyze the performances of our impervious surface dynamic time-series products,
470   four global 30 m multitemporal impervious surface products (GAIA, NUACI, GHSL and GlobeLand30) were selected as the comparative datasets. Figure 9 illustrates the total impervious area of five global impervious surface products on six continents over the period of 1985-2020. Overall, five global impervious surface products accurately captured the rational spatiotemporal trend over the past 35 years—the impervious surface area of all continents had steadily increased over time, and the increased impervious area in the Northern
475   Hemisphere was obviously greater than that in the Southern Hemisphere.

        Specifically, GISD30, GAIA, NUACI and GHSL showed great area-consistency in North America, while GlobeLand30 displayed a degree of overestimation, and its estimated area was almost 0.5×10^5 km^2 higher than that for other products. Furthermore, on the remaining five continents, GAIA showed the lowest total impervious area compared with the other global 30 m impervious products. Similarly, the comparison in Gong
480   et al. (2020) also indicated that GAIA showed the lowest impervious area among several global 30 m impervious surface products (NUACI, GHSL and GlobeLand30). As the NUACI only monitored the global urban dynamics and excluded the rural areas (Liu et al., 2018), it was expected that the total impervious areas given by NUACI would be lower than those given by GISD30, GHSL and GlobeLand30. As for GHSL, its impervious area varied greatly on different continents; for example, the total impervious area was close to that
485   of GISD30 in North America and Europe, of NUACI in Asia, South America and Oceania, and of GlobeLand30 in Africa. However, the impervious surface areas assessed by GHSL were generally lower than those of GISD30 and GlobeLand30. Lastly, GlobeLand30 gave the largest total impervious area for each continent, mainly because it also defined the vegetation in cities as artificial surfaces (Chen et al., 2015).
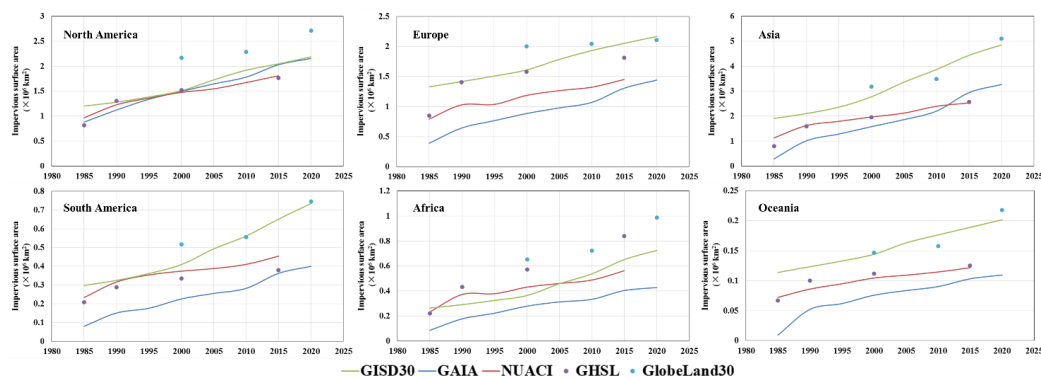
Figure 9. The impervious area of five global 30 m impervious surface products on six continents over the period of 1985-2020.

As the five global 30 m impervious surface products displayed large differences in estimated global total impervious area, it was necessary to further assess the performances of these products. Figure 10 illustrates the spatial patterns of these products after aggregation to the resolution of 0.05°. Clearly, there was great spatial consistency between the GISD30, GHSL and GlobeLand30 products—all of them accurately captured the actual patterns of global impervious surfaces, mainly those concentrated between approximately 20°N and 60°N. The NUACI products displayed the smallest impervious surface areas and the lowest intensity compared to the other products, especially in Europe and China, because it only identified urban pixels and excluded rural areas (Liu et al., 2018). Although the GAIA simultaneously identified urban and rural pixels, the impervious surface areas in Europe and Asia were significantly smaller than in the GISD30, GHSL and GlobeLand30 products. Furthermore, GHSL showed smaller impervious areas and a lower intensity than GISD30 and GlobeLand30 in India and China, the two most populous countries in the world. Lastly, as GlobeLand30 defined vegetation in cities as artificial surfaces (Chen et al., 2015), the impervious area given by GlobeLand30 for America was greater than that given by GISD30 and GHSL, because many cities in America display a serious mix of houses and vegetation.
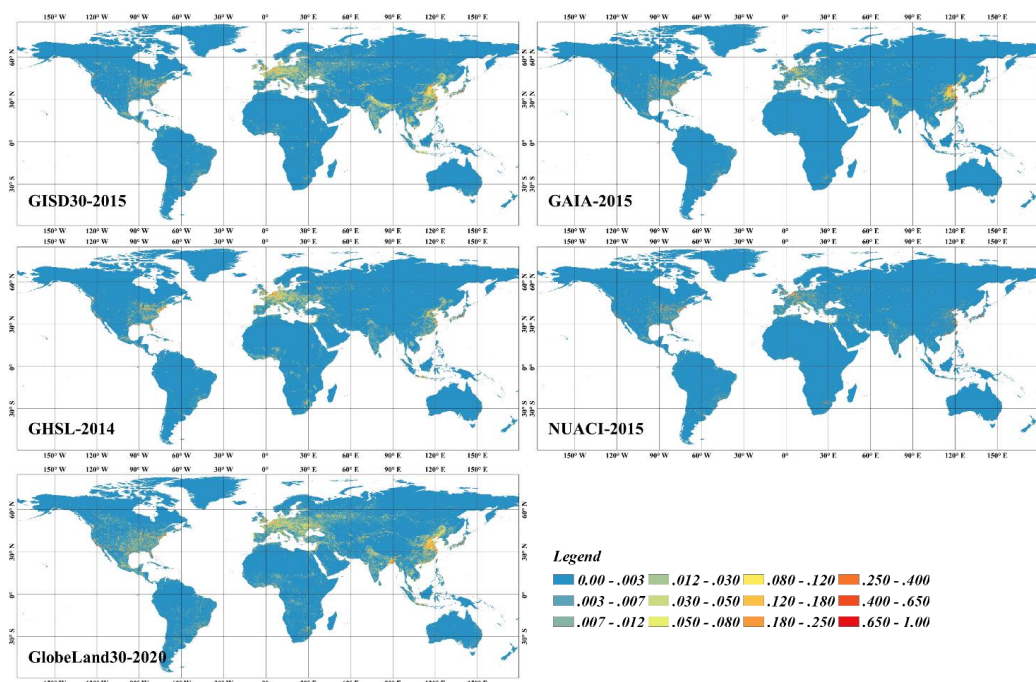
Earth System
Science
Data

Open Access

Discussions

Figure 10. The spatial patterns of five global 30 m impervious surface products after aggregation to the resolution of 0.5°.

To quantitatively analyze the consistency of five global 30 m impervious surface products, the
510 scatterplots of four products against GISD30 are illustrated in Figure 11. Firstly, the consistency between
GAIA and GISD30 increased with time, and the regression slope also approached 1. In 1985, most of the
points were concentrated below the 1:1 line, and the slope was much less than 1. However, by 2020, the
scatter plots were distributed on both sides of the 1:1 line, and showed great consistency, with an R^2 of 0.823
and an RMSE of 0.031. Secondly, as NUACI did not contain rural pixels, many scatter points were below the
515 1:1 line, and the consistency between NUACI and GISD30 was lower than that of the GAIA and GISD30
products (the maximum R^2 was 0.727). Further, as GlobeLand30 defined the vegetation in cities as artificial
surfaces (Chen et al., 2015), many scatter points were distributed above the 1:1 line, and the regression slopes
of the three periods were also close to 1. Lastly, there was greater agreement between GISD30 and GHSL than
between other products, especially for 2000, with the highest R^2 of 0.837, an RMSE of 0.025 and a regression
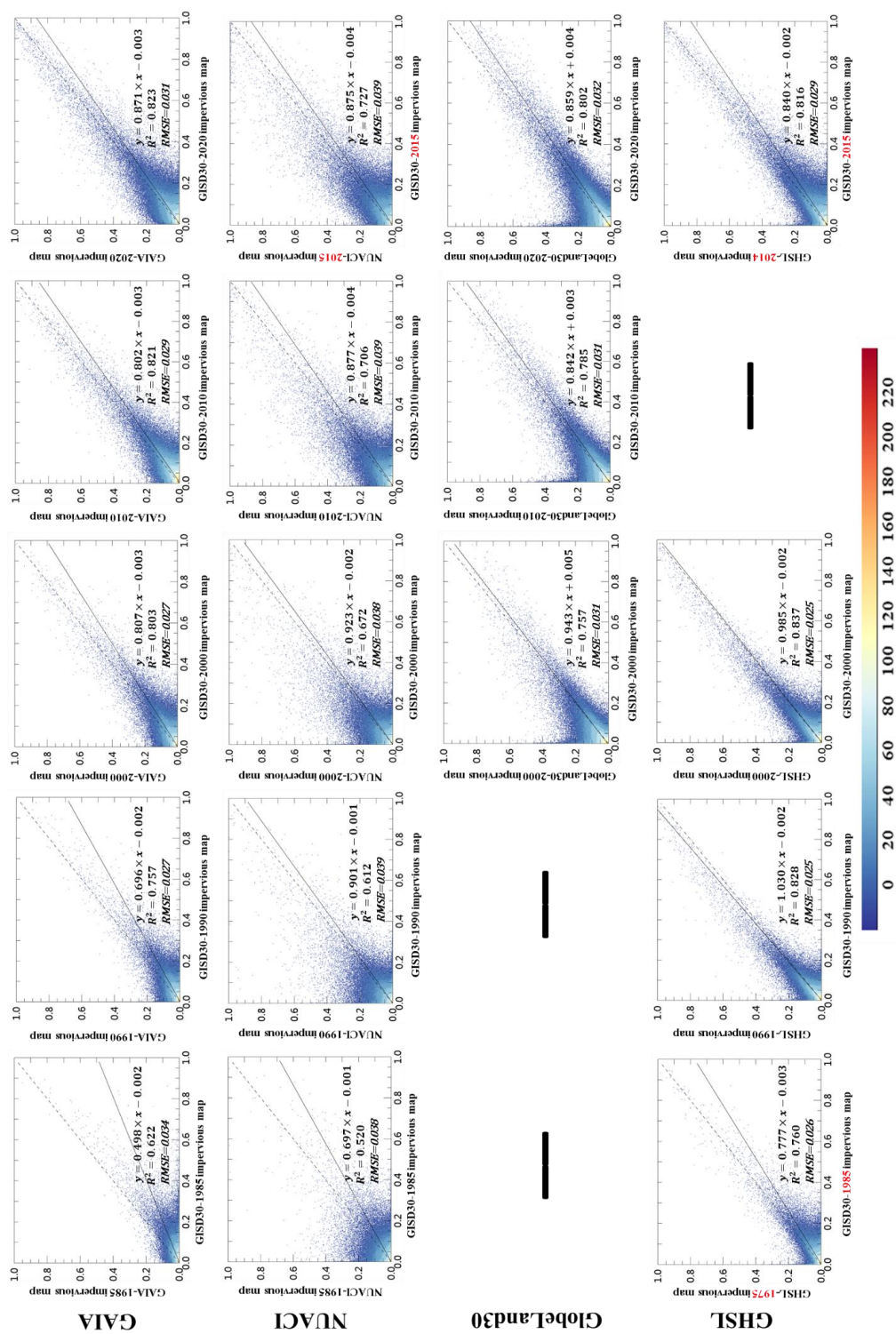520 slope of 0.985.

Figure 11. The scatter plots of four global 30 m impervious surface products compared to our GISD30 at the spatial resolution of 0.05°.

4.3.2 Cross-comparison at regional scale

525   To understand the performance of five global 30 m impervious surface products used for monitoring spatiotemporal dynamics, we randomly selected six cities after considering city size, spatial distribution and urban landscapes. Moscow and Shanghai were the representative mega cities, Bangkok and Jakarta were the cities in tropical regions (heavily affected by cloud and shadows), and Phoenix and Johannesburg were the representative cities for arid regions. Figure 12 illustrates the comparison between our GISD30 dynamic products and four comparative datasets for Moscow and Shanghai. NUACI suffered from overestimation for

530   two cities, misclassifying much vegetation as an impervious surface. It also failed to capture the expansion of impervious surfaces in Shanghai—many cropland pixels before 2000 were identified as impervious surfaces. The GAIA product misidentified some old urban pixels (green color) as newly expanded impervious surfaces (red color) in Moscow, and it overestimated the expansion of impervious surfaces from 2010 to 2020 in Shanghai. Specifically, according to the Landsat imagery, Shanghai's fastest urban

535   expansion occurred in 2000-2010, but the GAIA obviously lagged in this measurement. Furthermore, GHSL also could not accurately capture the spatiotemporal dynamics of impervious surfaces in detail. For example, it gave a low proportion of expanded impervious surfaces after 2000 in Shanghai, whereas in actuality, Shanghai experienced rapid urbanization after 2000. Lastly, although GlobeLand30 only measured the three epochs of 2000, 2010 and 2020 (its color scheme was different from other products), it showed a great

540   ability to capture the spatiotemporal expansion of impervious surfaces in two cities, and showed higher consistency with our GISD30 products.
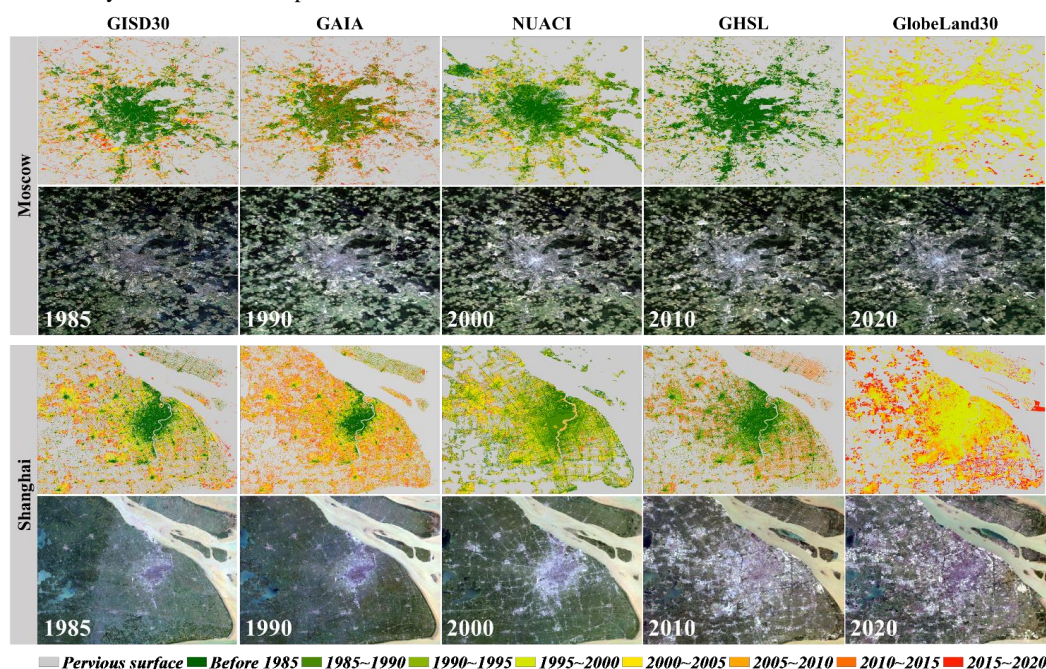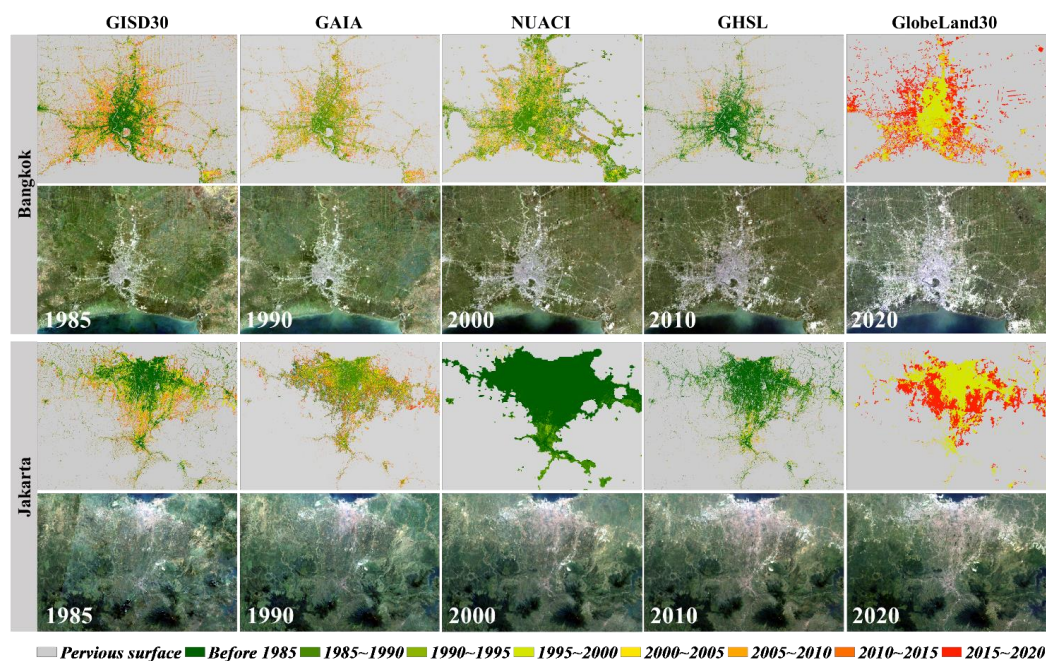

Figure 12. Comparisons between the GISD30 dynamic products and four other datasets (the GAIA products developed by Gong et al. (2020), the NUACI developed by Liu et al. (2018), the GHSL developed by

545   Florczyk et al. (2019), and the GlobeLand30 developed by Chen et al. (2015)) in the two representative

megacities of Moscow and Shanghai. In each case, the multi-epoch Landsat imagery, comprised by red, green and blue bands, came from the United States Geological Survey (https://earthexplorer.usgs.gov/).

Figure 13 illustrates the performances of five impervious surface products in two cloud-contaminated cities (Bangkok and Jakarta). Clearly, GISD30 performed the best in monitoring the spatiotemporal dynamics of the impervious surfaces in these two cities. Comparatively, GAIA clearly underestimated the impervious surfaces in Bangkok, and many small impervious surface objects in the peripheral cities (rural buildings) were missed. As regards impervious dynamics, GAIA underestimated the expansion after 2010 in Bangkok, and also failed to capture the expansion pattern from the city center to the outskirts in Jakarta. On the contrary, NUACI suffered from serious overestimation in two cities, and misidentified some croplands on the peripheries as impervious surfaces, especially in Jakarta. Meanwhile, it also failed to monitor the spatiotemporal dynamics of impervious surfaces in two cities, while the expansion area from 1985 to 2020 was severely underestimated and the impervious area before 2000 was overestimated. GHSL captured the distribution of impervious surfaces before 1985; however, the expansion of impervious surfaces over the past 35 years was seriously underestimated in two cities. Lastly, GlobeLand30 performed well in the city center, but it also missed many small impervious surface objects in the peripheral cities as a result of the minimum mapping unit of 4 × 4 pixels for each impervious object (Chen et al., 2015). In addition, GlobeLand30 performed better in Bangkok than in Jakarta when monitoring impervious surface expansion, because it overestimated the expansion from 2010 to 2020 in Jakarta.


Pervious surface | Before 1985 | 1985~1990 | 1990~1995 | 1995~2000 | 2000~2005 | 2005~2010 | 2010~2015 | 2015~2020

Figure 13. The comparisons between GISD30 and four reference datasets (the GAIA products developed by Gong et al. (2020), the NUACI developed by Liu et al. (2018), the GHSL developed by Florczyk et al. (2019), and the GlobeLand30 developed by Chen et al. (2015)) in the two cloud-contaminated cities of

Bangkok and Jakarta. In each case, the multi-epoch Landsat imagery, comprised by red, green and blue bands, came from the United States Geological Survey (https://earthexplorer.usgs.gov/).

570   Lastly, Figure 14 compares between our GISD30 and four reference products in two arid cities (Phoenix and Johannesburg). Overall, the highest consistency was found between GISD30 and GlobeLand30, because both accurately captured the spatial patterns of impervious surfaces and the expansion of impervious surfaces on the peripheries of cities. NUACI showed larger impervious areas than the other four products, but the corresponding Landsat imagery indicates that NUACI misidentified many

575   pervious surfaces (bare land) as impervious surfaces, especially in Johannesburg. Meanwhile, NUACI suffered an obvious stamping effect mainly caused by temporal differences among adjacent Landsat image sets, and also failed to capture the time of the expansion of impervious surfaces, especially in Johannesburg. GAIA performed well in identifying the impervious surface area and capturing the time of expansion in Phoenix, but it suffered from overestimation in the Johannesburg, where much arid bare land was wrongly

580   identified as an impervious surface in the early stages. Furthermore, as GHSL only covered the period of 1975-2014, it makes sense that it registered less expanded impervious surface than GISD30 and GlobeLand30. There was also great consistency between GHSL, GISD30 and GlobeLand30 for these two cities.
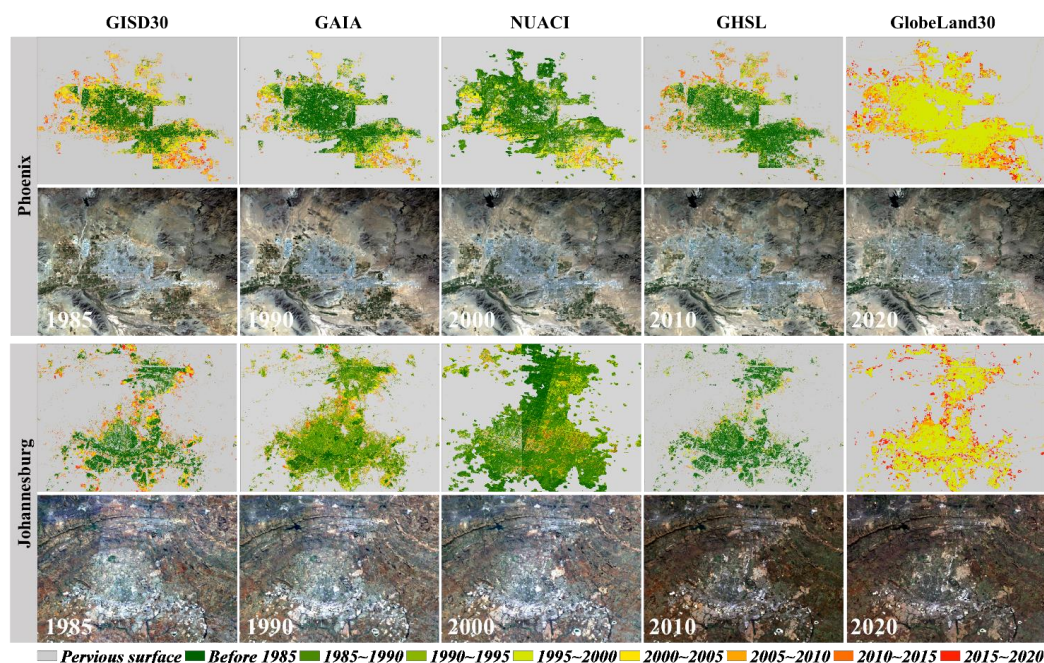
585   Figure 14. The comparisons between GISD30 and four reference datasets (the GAIA products developed by Gong et al. (2020), the NUACI developed by Liu et al. (2018), the GHSL developed by Florczyk et al. (2019), and the GlobeLand30 developed by Chen et al. (2015)) in the two representative arid cities of Phoenix and Johannesburg. In each case, the multi-epoch Landsat imagery, comprised by red, green and blue bands, came from the United States Geological Survey (https://earthexplorer.usgs.gov/).

590   **5   Discussion**

Earth System
Science
Data

Open Access

Discussions

5.1 Advantages of the proposed method for monitoring impervious surface dynamics

In contrast to traditional independent classification monitoring methods, which require expensive resources to collect multitemporal training samples (Gao et al., 2012; Zhang and Weng, 2016), we used prior global land-cover products and the spectral generalization strategy to automatically monitor the impervious surface dynamics. Specifically, as for the reliability of the training samples, the impervious layer in the GLC_FCS30-2020 land-cover products achieved a user's accuracy of 93.2% and a producer's accuracy of 94.8% (Zhang et al., 2020), and morphological filtering was also applied to further ensure the reliability of each sample in 2020. As it was difficult to assess the accuracy of all the training samples, we randomly selected 10,000 impervious surface samples from the global sample pool, and found that these impervious training samples achieved an accuracy of 95.52% in 2020. Therefore, the training samples derived in Section 3.2 were accurate enough for monitoring impervious surface dynamics.

In addition, contrary to other spectral generalization classification methods, which migrated the reflectance spectra of all land-cover types (Dannenberg et al., 2016; Phalke and Özdoğan, 2018; Zhang et al., 2019), we only migrated the reflectance spectra of impervious surfaces measured in 2020 to other periods, and simultaneously transferred the pervious samples to other periods based on the assumption of irreversibility. Therefore, we needed to independently train the classification models in each period using the migrated reflectance spectra of impervious and pervious surface samples. Correspondingly, our temporal adaptive models achieve better performances than traditional generalized models used for monitoring impervious surface dynamics. Furthermore, many studies have demonstrated that the spectral consistency between migrated spectra and classified imagery directly affects classification accuracy (Woodcock et al., 2001; Zhang et al., 2018). In this study, we used continuous Landsat imagery to preclude the effects of different sensors, and adopted a seasonally composited method with relative radiometric normalization to minimize the influence of temporal difference. Therefore, our temporally adaptive spectral generalization method was suitable for the impervious surface monitoring of long time-series.

5.2 Limitations and prospects of the global impervious surface dynamic dataset

In this study, we have proposed a novel automatic method to successfully produce a global 30 m impervious surface dynamic dataset over the period of 1985-2020, and quantitatively and qualitatively demonstrated that our dataset performed well in capturing the spatial distributions and spatiotemporal dynamics of impervious surfaces; however, there were still some weaknesses in our impervious surface dynamic products. Firstly, we assumed that the transition from pervious surface to impervious surface was irreversible over the monitoring period, which caused our method or product to fail to capture the transition from impervious to pervious surface (such as demolition caused by urban greening), as well as many changes that took place in impervious surfaces (such as urban demolition and reconstruction). Recently, Liu et al. (2019) used continuous change detection to successfully capture these reversible and multiple changes in Nanchang, China; however, the implementation efficiency of the method was low, and whether it can support the monitoring of global impervious surface dynamics remains to be verified. Therefore, our future work must exploit the advantages of a continuous change detection model to improve the effectivity of monitoring the spatiotemporal dynamics of impervious surfaces.

Our previous study (Zhang et al., 2020) quantitatively demonstrated that a combination of multisource remote sensing datasets could significantly improve the ability to recognize impervious surfaces, especially in semi-arid or arid regions, where bare land generally shares spectral characteristics with impervious

surfaces. In addition, the Landsat imagery available before 2000 was relatively sparse (illustrated in the Figure 1), which directly affects the monitoring accuracy of impervious surfaces, and this explains why the user's accuracy of the expansion of impervious surfaces before 2000 was significantly lower than after 2000
635   (Table 1). Similarly, Gong et al. (2020) also found that the availability of Landsat imagery had a positive relationship with impervious surface monitoring accuracy when creating GAIA global impervious surface products. Therefore, our future work should combine multisource remote sensing imagery (such as synthetic aperture radar (SAR), nighttime light (NTL) and AVHRR data) as auxiliary data to further improve impervious surface monitoring accuracy.

640   ## 6   Data availability

The global 30 m impervious surface dynamic dataset from 1985 to 2020 is free to access at http://doi.org/10.5281/zenodo.5220816 (Liu et al., 2021b). The global dynamic dataset was used to label the expansion information in a single band; specifically, the pervious surface and the impervious surface before 1985 were respectively labeled 0 and l, and the expanded impervious surfaces in the periods 1985-1990,
645   1990-1995, 1995-2000, 2000-2005, 2005-2010, 2010-2015 and 2015-2020 were labeled 2,3,4,5,6,7 and 8. Furthermore, in order to facilitate the use of these data, the global dynamic products were split into 961 5°×5° tiles in the GeoTIFF format, named "GISD30_1985-2020_E/W**N/S**.tif", where 'E/W**N/S**' is the latitude and longitude coordinates found in the upper left corner of the tile data.

7   Conclusion

650   In this study, a novel global 30 m impervious surface dynamic dataset for 1985 to 2020 was produced by combining time-series Landsat imagery and the spectral generalization method. Specifically, we first migrated the reflectance spectra of impervious surfaces, and simultaneously transferred the training samples of pervious surfaces to other periods, to automatically monitor the spatiotemporal dynamics of impervious surfaces from 1985 to 2020. Then, we combined the local adaptive modeling and time-series Landsat
655   imagery to independently produce impervious surface time-series products. Lastly, the spatiotemporal consistency checking method was applied to independent impervious surface products in order to minimize the effects of classification errors and ensure the reliability and spatiotemporal consistency of the final impervious surface dynamic dataset.

Overall, the global 30 m impervious surface dynamic dataset we produced accurately captured the
660   expansion pattern of impervious surfaces over the past 35 years. The quantitative results indicate that the global impervious surface area doubled in the past 35 years, from 5.116×10^5 km^2 in 1985 to 10.871×10^5 km^2 in 2020, and Asia underwent the greatest increase in impervious surface area compared to other continents, with a total increase of 2.946×10^5 km^2. Meanwhile, we also found that the expansion rate of impervious surface on six continents after 2000 was significantly faster than before 2000. In addition, the global 30 m
665   impervious surface dynamic dataset was validated by 18,540 multitemporal validation samples, and our dataset achieved the overall accuracy of 91.5% and a kappa coefficient of 0.866. Lastly, quantitative and qualitative comparisons between our GISD30 and four comparative impervious surface products (GAIA, GHSL, NUACI and GlobeLand30) indicate that our GISD30 products performed the best in capturing the spatial distributions and spatiotemporal dynamics of impervious surfaces. Therefore, it was concluded that
670   our global 30 m impervious surface dynamic dataset was an accurate product, and could provide vital support for monitoring regional or global urbanization or carrying out related tasks.

Acknowledgement

Financial support

References

Belgiu, M. and Drăguţ, L.: Random forest in remote sensing: A review of applications and future directions, ISPRS Journal of Photogrammetry and Remote Sensing, 114, 24-31, https://doi.org/10.1016/j.isprsjprs.2016.01.011, 2016.

Cai, S., Liu, D., Sulla-Menashe, D., and Friedl, M. A.: Enhancing MODIS land cover product with a spatial–temporal modeling algorithm, Remote Sensing of Environment, 147, 243-255, https://doi.org/10.1016/j.rse.2014.03.012, 2014.

Chen, J. and Chen, J.: GlobeLand30: Operational global land cover mapping and big-data analysis, Science China Earth Sciences, 61, 1533-1534, https://doi.org/10.1007/s11430-018-9255-3, 2018.

Chen, J., Chen, J., Liao, A., Cao, X., Chen, L., Chen, X., He, C., Han, G., Peng, S., Lu, M., Zhang, W., Tong, X., and Mills, J.: Global land cover mapping at 30m resolution: A POK-based operational approach, ISPRS Journal of Photogrammetry and Remote Sensing, 103, 7-27, https://doi.org/10.1016/j.isprsjprs.2014.09.002, 2015.

Chen, X., Cao, X., Liao, A., Chen, L., Peng, S., Lu, M., Chen, J., Zhang, W., Zhang, H., and Han, G.: Global mapping of artificial surfaces at 30-m resolution, Science China Earth Sciences, 59, 2295-2306, https://doi.org/10.1007/s11430-016-5291-y, 2016.

Chen, X., Liu, L., Zhang, X., Li, J., Wang, S., Liu, D., Duan, H., and Song, K.: An Assessment of Water Color for Inland Water in China Using a Landsat 8-Derived Forel–Ule Index and the Google Earth Engine Platform, IEEE Journal of Selected Topics in Applied Earth Observations and Remote Sensing, 14, 5773-5785, https://doi.org/10.1109/jstars.2021.3085411, 2021.

Corbane, C., Syrris, V., Sabo, F., Politis, P., Melchiorri, M., Pesaresi, M., Soille, P., and Kemper, T.: Convolutional neural networks for global human settlements mapping from Sentinel-2 satellite imagery, Neural Computing and Applications, 33, 6697-6720, https://doi.org/10.1007/s00521-020-05449-7, 2020.

Dannenberg, M., Hakkenberg, C., and Song, C.: Consistent Classification of Landsat Time Series with an Improved Automatic Adaptive Signature Generalization Algorithm, Remote Sensing, 8, 691, https://doi.org/10.3390/rs8080691, 2016.

Du, P., Samat, A., Waske, B., Liu, S., and Li, Z.: Random Forest and Rotation Forest for fully polarized SAR image classification using polarimetric and spatial features, Isprs Journal of Photogrammetry & Remote Sensing, 105, 38-53, https://doi.org/10.1016/j.isprsjprs.2015.03.002, 2015.

Florczyk, A., Corbane, C., Ehrlich, D., Freire, S., Kemper, T., Maffenini, L., Melchiorri, M., Pesaresi, M., Politis, P., and Schiavina, M.: GHSL Data Package 2019, Luxembourg. EUR, 29788 , https://doi.org/10.2760/290498, 2019.

Gao, F., Colstoun, E. B. d., Ma, R., Weng, Q., Masek, J. G., Chen, J., Pan, Y., and Song, C.: Mapping impervious surface expansion using medium-resolution satellite image time series: a case study in the Yangtze River Delta, China, International Journal of Remote Sensing, 33, 7609-7628, https://doi.org/10.1080/01431161.2012.700424, 2012.

Gislason, P. O., Benediktsson, J. A., and Sveinsson, J. R.: Random Forests for land cover classification, Pattern Recognition Letters, 27, 294-300, https://doi.org/10.1016/j.patrec.2005.08.011, 2006.

Gong, P., Li, X., Wang, J., Bai, Y., Chen, B., Hu, T., Liu, X., Xu, B., Yang, J., Zhang, W., and Zhou, Y.: Annual maps of global artificial impervious area (GAIA) between 1985 and 2018, Remote Sensing of Environment, 236, 111510, https://doi.org/10.1016/j.rse.2019.111510, 2020.

Gong, P., Li, X., and Zhang, W.: 40-Year (1978–2017) human settlement changes in China reflected by impervious surfaces from satellite remote sensing, Science Bulletin, doi: 10.1016/j.scib.2019.04.024, 2019. https://doi.org/10.1016/j.scib.2019.04.024, 2019.

Gorelick, N., Hancher, M., Dixon, M., Ilyushchenko, S., Thau, D., and Moore, R.: Google Earth Engine: Planetary-scale geospatial analysis for everyone, Remote Sensing of Environment, 202, 18-27, https://doi.org/10.1016/j.rse.2017.06.031, 2017.

Huang, X., Cao, Y., and Li, J.: An automatic change detection method for monitoring newly constructed building areas using time-series multi-view high-resolution optical satellite images, Remote Sensing of Environment, 244, 111802, https://doi.org/10.1016/j.rse.2020.111802, 2020.

Huang, X., Huang, J., Wen, D., and Li, J.: An updated MODIS global urban extent product (MGUP) from 2001 to 2018 based on an automated mapping approach, International Journal of Applied Earth Observation and Geoinformation, 95, 102255, https://doi.org/10.1016/j.jag.2020.102255, 2021.

Jin, H., Stehman, S. V., and Mountrakis, G.: Assessing the impact of training sample selection on accuracy of an urban classification: a case study in Denver, Colorado, International Journal of Remote Sensing, 35, 2067-2081, https://doi.org/10.1080/01431161.2014.885152, 2014.

Jing, C., Zhou, W., Qian, Y., Yu, W., and Zheng, Z.: A novel approach for quantifying high-frequency urban land cover changes at the block level with scarce clear-sky Landsat observations, Remote Sensing of Environment, 255, 112293, https://doi.org/10.1016/j.rse.2021.112293, 2021.

Kuang, W.: 70 years of urban expansion across China: trajectory, pattern, and national policies, Science Bulletin, 65, 1970-1974, https://doi.org/10.1016/j.scib.2020.07.005, 2020.

Li, X., Gong, P., and Liang, L.: A 30-year (1984–2013) record of annual urban dynamics of Beijing City derived from Landsat data, Remote Sensing of Environment, 166, 78-90, https://doi.org/10.1016/j.rse.2015.06.007, 2015.

Li, X., Zhou, Y., Zhu, Z., Liang, L., Yu, B., and Cao, W.: Mapping annual urban dynamics (1985–2015) using time series of Landsat data, Remote Sensing of Environment, 216, 674-683, https://doi.org/10.1016/j.rse.2018.07.030, 2018.

Liu, C., Zhang, Q., Luo, H., Qi, S., Tao, S., Xu, H., and Yao, Y.: An efficient approach to capture continuous impervious surface dynamics using spatial-temporal rules and dense Landsat time series stacks, Remote Sensing of Environment, 229, 114-132, https://doi.org/10.1016/j.rse.2019.04.025, 2019.

Liu, L., Zhang, X., Chen, X., Gao, Y., and Mi, J.: GLC_FCS30-2020:Global Land Cover with Fine Classification System at 30m in 2020 (v1.2), Zenodo [data]. https://doi.org/10.5281/zenodo.4280923, 2020a.

Liu, L., Zhang, X., Gao, Y., Chen, X., Shuai, X., and Mi, J.: Finer-Resolution Mapping of Global Land Cover: Recent Developments, Consistency Analysis, and Prospects, Journal of Remote Sensing, 2021, 1-38, https://doi.org/10.34133/2021/5289697, 2021a.

755 Liu, L., Zhang, X., Zhao, T., Gao, Y., Chen, X., and Mi, J.: GISD30: global 30-m impervious surface dynamic dataset from 1985 to 2020 using time-series Landsat imagery on the Google Earth Engine platform, Zenodo [data]. https://doi.org/ 10.5281/zenodo.5220816, 2021b.

Liu, X., Hu, G., Chen, Y., Li, X., Xu, X., Li, S., Pei, F., and Wang, S.: High-resolution multi-temporal mapping of global urban land using Landsat images based on the Google Earth Engine Platform, Remote Sensing of Environment, 209, 227-239, https://doi.org/10.1016/j.rse.2018.02.055, 2018.

760 Liu, X., Huang, Y., Xu, X., Li, X., Li, X., Ciais, P., Lin, P., Gong, K., Ziegler, A. D., Chen, A., Gong, P., Chen, J., Hu, G., Chen, Y., Wang, S., Wu, Q., Huang, K., Estes, L., and Zeng, Z.: High-spatiotemporal-resolution mapping of global urban change from 1985 to 2015, Nature Sustainability, 3, 564-570, https://doi.org/10.1038/s41893-020-0521-x, 2020b.

Mellor, A., Boukir, S., Haywood, A., and Jones, S.: Exploring issues of training data imbalance and mislabelling on random forest performance for large area land cover classification using the ensemble margin, ISPRS Journal of

765 Photogrammetry and Remote Sensing, 105, 155-168, https://doi.org/10.1016/j.isprsjprs.2015.03.014, 2015.

Okujeni, A., van der Linden, S., Tits, L., Somers, B., and Hostert, P.: Support vector regression and synthetically mixed training data for quantifying urban land cover, Remote Sensing of Environment, 137, 184-197, https://doi.org/10.1016/j.rse.2013.06.007, 2013.

Olofsson, P., Foody, G. M., Herold, M., Stehman, S. V., Woodcock, C. E., and Wulder, M. A.: Good practices for

770 estimating area and assessing accuracy of land change, Remote Sensing of Environment, 148, 42-57, https://doi.org/10.1016/j.rse.2014.02.015, 2014.

Pesaresi, M., Ehrlich, D., Ferri, S., Florczyk, A., Freire, S., Halkia, M., Julea, A., Kemper, T., Soille, P., and Syrris, V.: Operating procedure for the production of the Global Human Settlement Layer from Landsat data of the epochs 1975, 1990, 2000, and 2014, Publications Office of the European Union, 2016. 1-62, https://doi.org/10.2788/253582, 2016.

775 Phalke, A. R. and Özdoğan, M.: Large area cropland extent mapping with Landsat data and a generalized classifier, Remote Sensing of Environment, 219, 180-195, https://doi.org/10.1016/j.rse.2018.09.025, 2018.

Radoux, J., Lamarche, C., Van Bogaert, E., Bontemps, S., Brockmann, C., and Defourny, P.: Automated Training Sample Extraction for Global Land Cover Mapping, Remote Sensing, 6, 3965-3987, https://doi.org/10.3390/rs6053965, 2014.

780 Reba, M. and Seto, K. C.: A systematic review and assessment of algorithms to detect, characterize, and monitor urban land change, Remote Sensing of Environment, 242, 111739, https://doi.org/10.1016/j.rse.2020.111739, 2020.

Roy, D. P., Kovalskyy, V., Zhang, H. K., Vermote, E. F., Yan, L., Kumar, S. S., and Egorov, A.: Characterization of Landsat-7 to Landsat-8 reflective wavelength and normalized difference vegetation index continuity, Remote Sensing of Environment, 185, 57-70, https://doi.org/10.1016/j.rse.2015.12.024, 2016.

785 Roy, D. P., Wulder, M. A., Loveland, T. R., C.E., W., Allen, R. G., Anderson, M. C., Helder, D., Irons, J. R., Johnson, D. M., Kennedy, R., Scambos, T. A., Schaaf, C. B., Schott, J. R., Sheng, Y., Vermote, E. F., Belward, A. S., Bindschadler, R., Cohen, W. B., Gao, F., Hipple, J. D., Hostert, P., Huntington, J., Justice, C. O., Kilic, A., Kovalskyy, V., Lee, Z. P., Lymburner, L., Masek, J. G., McCorkel, J., Shuai, Y., Trezza, R., Vogelmann, J., Wynne, R. H., and Zhu, Z.: Landsat-8: Science and product vision for terrestrial global change research, Remote Sensing of Environment, 145,

790 154-172, https://doi.org/10.1016/j.rse.2014.02.001, 2014.

Schneider, A., Friedl, M. A., and Potere, D.: Mapping global urban areas using MODIS 500-m data: New methods and datasets based on 'urban ecoregions', Remote Sensing of Environment, 114, 1733-1746, https://doi.org/10.1016/j.rse.2010.03.003, 2010.

795 Schneider, A., Friedl, M. A., and Potere, D.: A new map of global urban extent from MODIS satellite data, Environmental Research Letters, 4, 044003, https://doi.org/10.1088/1748-9326/4/4/044003, 2009.

Science, A. A. f. t. A. o.: Rise of the City, Science, 352, 906-907, https://doi.org/10.1126/science.352.6288.906, 2016.

Sexton, J. O., Song, X.-P., Huang, C., Channan, S., Baker, M. E., and Townshend, J. R.: Urban growth of the Washington, D.C.–Baltimore, MD metropolitan region from 1984 to 2010 by annual, Landsat-based estimates of impervious cover, Remote Sensing of Environment, 129, 42-53, https://doi.org/10.1016/j.rse.2012.10.025, 2013.

800 Song, X.-P., Sexton, J. O., Huang, C., Channan, S., and Townshend, J. R.: Characterizing the magnitude, timing and duration of urban growth from time series of Landsat-based estimates of impervious cover, Remote Sensing of Environment, 175, 1-13, https://doi.org/10.1016/j.rse.2015.12.027, 2016.

Sun, Z., Xu, R., Du, W., Wang, L., and Lu, D.: High-Resolution Urban Land Mapping in China from Sentinel 1A/2 Imagery Based on Google Earth Engine, Remote Sensing, 11, 752, https://doi.org/10.3390/rs11070752, 2019.

805 USGS: Landsat 8 surface reflectance code (LaSRC) product, Department of the Interior U.S. Geological Survey, available at: https://www.usgs.gov/media/files/land-surface-reflectance-code-lasrc-product-guide (last access: 21 August 2021), 2017.

Vermote, E.: LEDAPS surface reflectance product description, available at: https://www.usgs.gov/media/files/landsat-4-7-collection-1-surface-reflectance-code-ledaps-product-guide (last 810 access: 21 Auguest 2021), 2007.

Vermote, E., Justice, C., Claverie, M., and Franch, B.: Preliminary analysis of the performance of the Landsat 8/OLI land surface reflectance product, Remote Sensing of Environment, 185, 46-56, https://doi.org/10.1016/j.rse.2016.04.008, 2016.

Weng, Q.: Remote sensing of impervious surfaces in the urban areas: Requirements, methods, and trends, Remote 815 Sensing of Environment, 117, 34-49, https://doi.org/10.1016/j.rse.2011.02.030, 2012.

White, J. C., Wulder, M. A., Hobart, G. W., Luther, J. E., Hermosilla, T., Griffiths, P., Coops, N. C., Hall, R. J., Hostert, P., Dyk, A., and Guindon, L.: Pixel-Based Image Compositing for Large-Area Dense Time Series Applications and Science, Canadian Journal of Remote Sensing, 40, 192-212, https://doi.org/10.1080/07038992.2014.945827, 2014.

Woodcock, C. E., Macomber, S. A., Pax-Lenney, M., and Cohenc, W. B.: Monitoring large areas for forest change 820 using Landsat: Generalization across space, time and Landsat sensors, Remote Sensing of Environment, 78, 194–203, https://doi.org/10.1016/S0034-4257(01)00259-0, 2001.

Wu, C.: Normalized spectral mixture analysis for monitoring urban composition using ETM+ imagery, Remote Sensing of Environment, 93, 480-492, https://doi.org/10.1016/j.rse.2004.08.003, 2004.

Xie, Y. and Weng, Q.: Spatiotemporally enhancing time-series DMSP/OLS nighttime light imagery for assessing 825 large-scale urban dynamics, ISPRS Journal of Photogrammetry and Remote Sensing, 128, 1-15, https://doi.org/10.1016/j.isprsjprs.2017.03.003, 2017.

Zhang, H. K. and Roy, D. P.: Using the 500 m MODIS land cover product to derive a consistent continental scale 30 m Landsat land cover classification, Remote Sensing of Environment, 197, 15-34, https://doi.org/10.1016/j.rse.2017.05.024, 2017.

830 Zhang, L. and Weng, Q.: Annual dynamics of impervious surface in the Pearl River Delta, China, from 1988 to 2013, using time series Landsat imagery, ISPRS Journal of Photogrammetry and Remote Sensing, 113, 86-96, https://doi.org/10.1016/j.isprsjprs.2016.01.003, 2016.

Zhang, X., Liu, L., Chen, X., Gao, Y., Xie, S., and Mi, J.: GLC_FCS30: global land-cover product with fine classification system at 30 m using time-series Landsat imagery, Earth Syst. Sci. Data, 13, 2753-2776, https://doi.org/10.5194/essd-13-2753-2021, 2021.

Zhang, X., Liu, L., Chen, X., Xie, S., and Gao, Y.: Fine Land-Cover Mapping in China Using Landsat Datacube and an Operational SPECLib-Based Approach, Remote Sensing, 11, 1056, https://doi.org/10.3390/rs11091056, 2019.

Zhang, X., Liu, L., Wang, Y., Hu, Y., and Zhang, B.: A SPECLib-based operational classification approach: A preliminary test on China land cover mapping at 30 m, International Journal of Applied Earth Observation and Geoinformation, 71, 83-94, https://doi.org/10.1016/j.jag.2018.05.006, 2018.

Zhang, X., Liu, L., Wu, C., Chen, X., Gao, Y., Xie, S., and Zhang, B.: Development of a global 30 m impervious surface map using multisource and multitemporal remote sensing datasets with the Google Earth Engine platform, Earth Syst. Sci. Data, 12, 1625-1648, https://doi.org/10.5194/essd-12-1625-2020, 2020.

Zhao, M., Zhou, Y., Li, X., Cheng, W., Zhou, C., Ma, T., Li, M., and Huang, K.: Mapping urban dynamics (1992−2018) in Southeast Asia using consistent nighttime light data from DMSP and VIIRS, Remote Sensing of Environment, 248, 111980, https://doi.org/10.1016/j.rse.2020.111980, 2020.

Zhou, Y., Li, X., Asrar, G. R., Smith, S. J., and Imhoff, M.: A global record of annual urban dynamics (1992−2013) from nighttime lights, Remote Sensing of Environment, 219, 206-220, https://doi.org/10.1016/j.rse.2018.10.015, 2018.

Zhu, Z., Gallant, A. L., Woodcock, C. E., Pengra, B., Olofsson, P., Loveland, T. R., Jin, S., Dahal, D., Yang, L., and Auch, R. F.: Optimizing selection of training and auxiliary data for operational land cover classification for the LCMAP initiative, ISPRS Journal of Photogrammetry and Remote Sensing, 122, 206-221, https://doi.org/10.1016/j.isprsjprs.2016.11.004, 2016.

Zhu, Z. and Woodcock, C. E.: Automated cloud, cloud shadow, and snow detection in multitemporal Landsat data: An algorithm designed specifically for monitoring land cover change, Remote Sensing of Environment, 152, 217-234, https://doi.org/10.1016/j.rse.2014.06.012, 2014.

Zhu, Z., Zhang, J., Yang, Z., Aljaddani, A. H., Cohen, W. B., Qiu, S., and Zhou, C.: Continuous monitoring of land disturbance based on Landsat time series, Remote Sensing of Environment, doi: 10.1016/j.rse.2019.03.009, 2019. https://doi.org/10.1016/j.rse.2019.03.009, 2019.

Zhuo, L., Shi, Q., Tao, H., Zheng, J., and Li, Q.: An improved temporal mixture analysis unmixing method for estimating impervious surface area based on MODIS and DMSP-OLS data, ISPRS Journal of Photogrammetry and Remote Sensing, 142, 64-77, https://doi.org/10.1016/j.isprsjprs.2018.05.016, 2018.